Exploring substrate binding in the extracellular vestibule of MhsT by atomistic simulations and Markov models

Ara M. Abramyan[1], **Matthias Quick**[2,4], **Catherine Xue**[1], **Jonathan A. Javitch**[2,3,4], and **Lei Shi**[1,*]

[1]Computational Chemistry and Molecular Biophysics Unit, National Institute on Drug Abuse - Intramural Research Program, National Institutes of Health, Baltimore, Maryland, 21224, United States

[2]Departments of Psychiatry Columbia University College of Physicians and Surgeons, New York, New York, 10032, United States

[3]Pharmacology, Columbia University College of Physicians and Surgeons, New York, New York, 10032, United States

[4]Division of Molecular Therapeutics, New York State Psychiatric Institute, New York, New York, 10032, United States

Abstract

Neurotransmitter:sodium symporters (NSS) terminate neurotransmission through Na^+-driven reuptake of cognate neurotransmitters. Crystallographically, whereas both substrates and inhibitors have been found to bind in the central binding (S1) site of NSS, inhibitors were found to bind to a second binding (S2) site in the extracellular vestibule (EV) of transporters for leucine (LeuT) and serotonin. Based on computational and experimental studies, we proposed that substrates bind to the S2 site of LeuT as well, and that substrate binding to the S2 site is essential for Na^+-coupled symport. Recent binding experiments show that substrate (L-Trp) binding in the S2 site of MhsT, another bacterial NSS, is also central to the allosteric transport mechanism. Here, we used extensive molecular dynamics simulations combined with Markov state model analysis to investigate the interaction of L-Trp with the EV of MhsT, and identified potential binding poses of L-Trp as well as induced conformational changes in the EV. Our computational findings were validated by experimental mutagenesis studies, and shed light on the ligand binding characteristics of the EV of NSS, which may facilitate development of allosteric ligands targeting NSS.
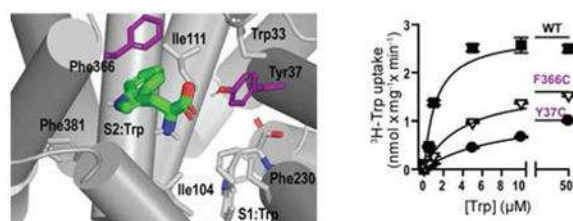
Graphical abstract

INTRODUCTION

Neurotransmitter:sodium symporters (NSS) play an essential role in neurotransmission and include transporters for serotonin and dopamine (SERT and DAT), which are targets for antidepressants and abused psychostimulants. In a process that involves traversing between outward-facing and inward-facing conformational states, these transporters terminate neurotransmission through Na^+-driven reuptake of their cognate neurotransmitters.[1]

The transport process can be modulated by both competitive and allosteric inhibitors. The crystal structures of NSS revealed a central binding (S1) site (Figure 1A) that binds both substrates and competitive inhibitors.[2–5] For example, cocaine and benztropines bind in the S1 site of DAT, and has been found to competitively inhibit DAT.[2, 6, 7] For the SERT inhibitor citalopram, in addition to the high-affinity binding in the S1 site of SERT, a low-affinity allosteric binding site has been known to exist, and occupation of this site slows the dissociation rate of the ligand from the S1 site.[8, 9] A recent crystal structure of SERT (PDB ID: 5I73) demonstrated that the likely location of this allosteric site for S-citalopram is in the extracellular vestibule (EV) (Figure S1A).[4] Interestingly, the EV also accommodates the binding pockets for several LeuT inhibitors as well (Figure S1B).[5, 10–12]

The substrate serotonin was shown to slow the dissociation of imipramine from SERT, suggesting the existence of an allosteric substrate binding site for serotonin in the dissociation pathway of the S1-bound imipramine.[13] Computational and experimental studies in LeuT, a bacterial NSS homolog, have shown that the binding of substrate in a subpocket of the EV (termed the S2 site) triggers conformational transition towards an inward-facing state, facilitating substrate release from the S1 site.[14, 15]

The recent crystal structures of MhsT (PDB IDs: 4US3 and 4US4),[16] another bacterial NSS, were solved in an inward-occluded conformation,[17] with a substrate (L-Trp)-occupied S1 site and a collapsed EV. Saturation binding studies in n-dodecyl-β-D-maltopyranoside (DDM), the detergent used for the crystallization of MhsT, supported a molar binding stoichiometry of 1. However, binding studies performed with MhsT purified in n-decyl-β-D-maltopyranoside (DM), or with MhsT reconstituted into nanodiscs showed that this NSS member features a 2:1 substrate binding stoichiometry under equilibrium conditions. Mutational analyses and site-directed thiol-labeling studies reveal that the EV in MhsT indeed accommodates an S2 site that is essential for transport, just like LeuT.[18] These recent findings prompted us to investigate substrate binding in the EV and the resulting conformational changes using extensive molecular dynamics (MD) simulations combined with Markov state model (MSM) analysis.

RESULTS and DISCUSSION

Based on a previously equilibrated MhsT model,[17] after initial docking of a L-Trp into the EV (S2:Trp) in the presence of a L-Trp in the S1 site (S1:Trp), we carried out five rounds of MD simulations that were guided by MSM analysis after each round (see Methods). In the MSM analysis, the interacting residues of S2:Trp were identified for each frame of the MD simulations, and the identities of these residues were used as input features to build the MSM (see Methods and Figures S4 and S5). In our final MSM analysis of more than 56 μs of accumulated MD data, we identified twelve S2:Trp-bound metastable states (MSs) (Figure 1). The six MSs with the largest equilibrium probabilities account for 84% of total equilibrium probability, and are the focus of our following analysis (Figure 1B-H and Table 1).

Among the six largest MSs, the S2:Trp poses in the red and orange MSs (red and orange poses) occupy more extracellular positions in the EV further away from the S1:Trp, compared to the brown, cyan, blue, and green poses (Figure S2A). Specifically, the orange pose occupies a sub-pocket between the extracellular portions of transmembrane segments (TMs) 1 and 6 (TM1e and TM6e respectively, see Figure S3 for our subsegment divisions of MhsT), whereas the red pose is in close proximity to extracellular loop 4 (EL4) (Figure 1E, H). The brown pose appears to occupy the region between EL4 and TM10e (Figure 1G), representing a transition pose between the more extracellular poses (orange and red) and the poses closer to the S1 site (cyan, blue, green). In both the cyan and blue poses, the indole ring of S2:Trp is perpendicular to the plane of membrane and its amine and carboxylic groups form salt bridge interactions with Asp385 and Arg34, respectively (Figure 1D, F). The green pose, which has the largest equilibrium probability, is distinct in that the indole ring of S2:Trp is relatively parallel to the plane of the membrane and is positioned closer to TM10e and EL5 (Figure 1C).

Interestingly, we observed that the presence of S2:Trp gradually induced significant conformational changes in the EV of MhsT. In a representative trajectory shown in movie S1 in Supporting Information, the S2:Trp transitioned from the brown to the blue pose, and was then stabilized in the green pose (Figure S2B). This transition was accompanied by coordinated movements in the EV, especially near the TM10e subsegment.

To quantify such changes, we calculated structural differences at both subsegment and residue levels between the most dominant green MS and the S2:*apo* condition (the data of which were extracted from ref [17]) using pairwise interaction analyzer for MhsT (PIA-MhsT, see Methods). At the subsegment level, the results of our analysis indicate that the most prominent changes are the rearrangement of EL5 and TM10e on the extracellular side (Figure 2A). Indeed, when we further calculated the distance between TM10e and TM1e in various conditions, the large differences and fluctuations of this distance demonstrate significant flexibility of TM10e, which showed substantial conformational changes upon S2:Trp binding (Figure 3).

Specifically, at the residue level, we observed significantly larger distances from Phe381 of TM10e to other S2:Trp-interacting residues in the green MS, while Phe366 of EL5 moves

closer to other residues, suggesting coordinated rearrangement between these two regions upon S2:Trp binding (Figure 2B). A further analysis of the dihedral angles of these residues showed that they are highly dynamic (movie S1). In particular, in the presence of the bound S2:Trp, the sidechain of Phe381 makes a counter-clock wise rotation in the green MS from the S2:*apo* condition (Figure 4A, D). In the two-fold pseudosymmetry of the LeuT structural fold, TM10e is at a peripheral position from the center of the transmembrane domain and is expected to have substantial flexibility – indeed the subsegment below TM10e, TM10m, is in a bulge conformation that may allow such flexibility.[19] Interestingly, TM5i and TM5m, which are pseudosymmetrical to TM10e and TM10m, undergo drastic rearrangement from an unwound to a structured configuration during conformational transitions in MhsT.[16, 17] In addition, significant conformational changes of TM10 have been observed crystallographically in other transporters with the LeuT-like structure fold, such as Mhp1.[20]

How is the observed rotation of TM10e coupled to the S1 site? Compared to the S2:*apo* condition, we found that the changes in TM10e propagate downwards towards the S1 site through the rotamer changes of Asp385 of TM10e and Ser389 of TM10m, which are associated with the rearrangement of an S1:Trp interacting Met236 of TM8m (Figure 4E-G).

Residues such as Phe381 that play a significant role in conformational transitions are expected to be critical for S2:Trp binding. Indeed, the F381C mutation in MhsT completely eliminated S2 binding and substrate transport,[18] as did the mutation of the aligned residue in LeuT, Leu400.[14]

The complete elimination of S2 substrate binding by the F381C mutation is likely due both to its disruption of S2-ligand binding as well as impaired conformational transition. To further characterize the S2 substrate binding site *per se*, we chose Tyr37 and Phe366 for mutagenesis. These two residues interact with the S2:Trp in the highly populated MSs (Table 1) but appear not to be critical in conformational transitions (Figure 4A): specifically in the green MS, Phe366 stacks with the indole ring of S2:Trp (Figure 4A, C), while the carbonyl group of S2:Trp hydrogen bonds with Tyr37 (Figure 4A).

Interestingly, the Y37C and F366C mutations resulted in biphasic binding curves (Figure 5). This observation is in stark contrast to the binding isotherm of MhsT-WT (Figure 5A), which was well fit to a rectangular hyperbola reaching a molar Trp:MhsT binding ratio of 2.[18] Rectangular hyperbolic isotherms have been described for LeuT-fold proteins where both substrate binding sites exhibit similar affinities, whereas more complex (i.e., biphasic) binding isotherms have been observed when the affinities in both sites differ by a factor of about 10[14, 21–23] (Figure 5B, C), suggesting that in the Y37C and F366C mutants, the S2 site has a lower affinity than that in the WT. Such disrupted S2 binding results in substantially reduced ^{3}H-Trp transport as reflected in lowered initial rates and V_{max} values of ^{3}H-Trp transport as well (Figure 6).

Trp33 is a highly conserved residue among the NSS members in the EV, and was suggested to replace the role of the movable substrate in the S2 site.[16] However, recent results[18] indicate that, whereas Trp33 is not essential for Na$^+$-coupled symport, a conformational arrangement that repositions its side chain may enable a Trp substrate molecule to bind in

the S2 site, a critical step in the allosteric mechanism of transport. Interestingly, among the six MSs with the largest equilibrium probability, Trp33 in the green MS does not directly interact with S2:Trp, and we observed a significant change of the rotamer of Trp33 in this MS compared to the S2:*apo* condition and the crystal structure (Figure 4A, B). With all the experimental results considered, including both from our previous study[18] and the Y37C and F366C results herein, we infer that the green pose is most consistent with all the experimental findings in representing the S2 binding pose. Thus, the opening of TM10e upon substrate binding appears to be an important conformational rearrangement required for the formation of the S2 binding site. As MhsT is an 11-TM transporter, its TM10e and TM10m are directly exposed to lipids. The lack of intramolecular restraints on TM10e in the transmembrane domain of 11-TM MhsT, such as those between TM10e and TM12 in the 12-TM NSS, might allow us to observe the changes in the microsecond-scale MD simulations. Nevertheless, this does not imply that this potentially functionally important rearrangement of TM10 does not happen in the 12-TM NSS.

CONCLUSIONS

Taken together, by combining extensive MD simulations and MSM analysis of the substrate Trp binding to the EV of MhsT, we have identified several potential binding poses of S2:Trp. In particular, the green pose best explains all our experimental findings. However, given the complexity of the transport cycle in which MhsT has to traverse several conformational states, further investigation is required to fully reveal mechanistic consequences of S2:Trp binding.

Targeting the S2 site of NSS is a promising strategy for designing allosteric modulators of transport. Our findings can be used to inform the design of new S2 compounds, as well as our understanding of the subsequent events in the transport mechanism.

METHODS

MD simulations.

The starting MhsT model for our MD simulations was based on the S1:Trp-bound crystal structure of MhsT (PDB ID: 4US4). A second Trp molecule was docked in the S2 site using the induced-fit docking (IFD) protocol[24] implemented in the Schrodinger suite (release 2014–4).

Visual Molecular Dynamics (VMD) program[25] was used to prepare the simulation systems: the selected MhsT model from IFD was immersed in explicit POPC membrane bilayer and water solvent environment; Na^+ and Cl^- ions corresponding to 0.15 M concentration were added in the water phase.

The energy minimization and MD simulations were carried out using NAMD[26] with the CHARMM36 force field.[27, 28] A cutoff of 12 Å was used for the nonbonded interactions, and long-range electrostatic effects were evaluated by the particle mesh Ewald method. The system was initially minimized for 6000 steps. In the following MD simulations, the hybrid Nose-Hoover Langevin piston method[29] was used to maintain constant pressure at 1 atm on

an anisotropic flexible periodic cell, for which a constant-ratio constraint was applied in the X-Y plane. Constant temperature at 310 K was maintained with Langevin dynamics in the isothermal-isobaric (NPT) ensemble. For the first 200 ps of the first round of MD simulations (see below), a time step of 1 fs was used, which was then increased to 2 fs for the rest of the simulations.

MSM analysis.

We used the pyEMMA program (version 2.3.2)[32] to perform the MSM analysis[30, 31] as described previously,[33–35] and used the binary features that describe the contacts between S2:Trp and MhsT as the input features. Specifically, if the shortest heavy-atom distance between S2:Trp and any given residue of the protein was within 5Å, the contact to that residue was set to 1, otherwise 0. Thus for MhsT that has 453 residues, each MD frame was represented by a 453-dimentional binary feature vector.

The time-lagged independent component analysis (TICA)[36, 37] was used to estimate the slow linear subspace of the input features. A dimension reduction was achieved by projecting the feature vectors on the 25 slowest TICA components (representing 80% of the cumulative kinetic variance[38]). k-means clustering was then used to partition the subspace into 25, 50, 100, 200, or 1000 microstates. The 50-state MSM had the highest score in terms of the variational principle,[39, 40] as determined by using a previously described cross-validation protocol (Table S1).[35] For this MSM, the implied timescales (ITSs)[41] for the transitions among microstates as a function of various lag times are shown in Figure S4. At each lag time, we employed the Bayesian sampling to compute statistical uncertainties of 500 transition matrix samples. Convergences of ITSs were achieved at a lag time of 120 ns, which was then consistently used for further analyses. We used the PCCA++ method[42] to coarse-grain the microstates into MSs. The kinetic analysis was performed on those microstates having >60% of probability to belong to a particular MS. The final MSM was shown to be converged using Chapman-Kolmogorov test (Figure S5).[31]

MSM-guided iterative MD sampling.

To adequately sample the S2:Trp binding modes and the conformations exhibited by MhsT in various binding modes, we used an iterative MD sampling protocol, and carried out totally 5 rounds of MD simulations based on the MSM analysis. Specifically, in the first round of MD simulations, we initiated three trajectories starting with different random seeds. By taking advantage of the MSM analysis after each round, we analyzed the population of microstates and restarted four rounds of simulations from those microstates having the smallest populations, with reducing lengths of simulations.[33, 35, 43] The minimum length of trajectories was 300 ns. Overall, we collected 44 MD trajectories with an aggregated simulation time of 56.7 μs.

Conformational analysis.

The data sets for the conformational analysis were assembled as following: for each of the S2:Trp-bound MSs, we randomly extracted 1000 MD frames from the microstates that have >60% probability to belong to a given MS; for the equilibrated S2:apo condition, we

randomly extracted 1000 frames from our previous simulation trajectories of MhsT without S2:Trp.[44]

We used MDTraj (version 1.7.2)[45] in combination with *in-house* Python scripts to calculate distances and dihedral angles.

We developed the pairwise interaction analyzer for MhsT (PIA-MhsT), based on our previously developed PIA-GPCR[46] and PIA-DAT.[35] For the analysis of coarse-grained interaction network of MhsT at subsegment level, we used the following structural elements as previously defined:[17] NT (N terminus, residues 1–13), TM1i (the intracellular section (i) of TM1, 14–23), TM1m (the middle section (m) of TM1, 24–31), TM1e (the extracellular section (e) of TM1, 32–41), EL1 (42–44), TM2e (45–50), TM2m (51–60), TM2i (61–74), IL1 (the intracellular loop 1, 75–87), TM3i (88–103), TM3m (104–108), TM3e (109–124), EL2 (125–146), TM4e (147–155), TM4i (156–164), IL2 (165–171), TM5i (172–175), TM5m (176–181), TM5e (182–194), EL3 (195–217), TM6e (218–226), TM6m (227–238), TM6i (239–245), IL3 (246–252), TM7i (253–262), TM7m (263–269), TM7e (270–282), EL4a (283–288), EL4b (289–305), TM8e (306–319), TM8m (320–328), TM8i (329–338), IL4 (339–343), TM9i (344–353), TM9e (354–364), EL5 (365–379), TM10e (380–387), TM10m (388–392), TM10i (393–405), IL5 (406–426), and TM11 (427–448).

In a MD frame, if the shortest heavy-atom distance between S2:Trp and any given residue of the protein was within 5Å, we defined that S2:Trp forms an interaction with this residue. The S2:Trp interacting residues for a given MS were defined to be those having frequencies of interaction with S2:Trp that are above 50% (Table 1).

Site-directed mutagenesis, gene expression, protein purification.

PCR-based site-directed mutagenesis was used to replace Tyr37 or Phe366 in the *mhsT* gene in plasmid pQO6-TEV.[16] Verified mutated genes were transferred to a pNZ8048 derivative and expressed in *Lactococcus lactis* NZ9000 and purified to apparent homogeneity (see Fig. 5D) in 50 mM 2-amino-2-(hydroxymethyl)-1,3-propanediol (Tris)/2-(*N*-morpholino)-ethanesulfonic acid (Mes), pH 7.5/20% glycerol/150 mM NaCl/1 mM Tris(2-carboxyethyl) phosphine (TCEP)/0.1 % (w/v) n-decyl-β-D-maltopyranoside (DM) as previously described.[18, 47] Protein concentration was measured with the amidoblack protein assay.[48]

Transport assay.

L-[^{3}H]tryptophan (American Radiolabeled Chemicals, Inc) transport was measured in intact *E. coli* MQ614 harboring pQE60 (serving as control) or pQE60 derivatives containing the *mhsT*-WT, -Y37C, or -F366C in buffer composed of 10 mM Tris/Mes, pH 8.5/50 mM NaCl[16]. Western blotting (using a monoclonal antibody against the N-terminal His tag present in all MhsT constructs) was used to determine the relative amounts of the respective MhsT variants in the membrane of MQ614 and showed that the mutations do not significantly alter the expression or insertion of the protein in the *E. coli* plasma membrane (Fig. 6C). Membrane vesicles were produced from MQ614 cells expressing the given *mhsT* variants or those transformed with pQE60 (no *mhsT*). 10 μg of total membrane protein were subjected to SDS-PAGE followed by immunoblot analysis using His probe (Santa Cruz

Biotechnology, Inc.) and horseradish peroxidase-based chemiluminescence detection (SuperSignal® West Pico kit, Thermo Scientific).

Scintillation proximity assay (SPA)-based binding studies.

SPA-based L-[^{3}H]tryptophan binding to purified MhsT was performed in 50 mM Tris/Mes, pH 7.5/20% glycerol/150 mM NaCl/1 mM TCEP/0.1% DM or DDM. 50 ng protein were bound to Cu^{2+}-coated yttrium silicate (YSi) SPA beads (2.5 mg/mL) in 100 µL in the dark for 16 h at 4 °C with vigorous shaking. The binding activity was determined with a Wallac 1450 MicroBeta™ plate PMT counter in the SPA mode.

The non-proximity background signal was determined in the presence of 800 mM imidazole to prevent the interaction of the His-tagged protein with the Cu^{2+}-coated SPA beads. Thus, specific binding was determined by subtracting the nonspecific binding from the total binding. Nonlinear regression fitting of the data (mean ± S.E.M. of triplicate determinations) of a representative experiment (n ≥2) was performed in Prism 7 to obtain the EC_{50} and molar ratios of ligand-to-MhsT binding by plotting specific binding as function of free Trp. The binding isotherm for MhsT-WT was determined by fitting the data to a one-site binding model, whereas data fits of the two phases observed for MhsT-Y37C and -F366C were performed independently with one-site models.

Data analysis.

All experiments were performed at least in duplicate with replicas of ≥3 and data are expressed as mean ± S.E.M.

Supplementary Material

Refer to Web version on PubMed Central for supplementary material.

ACKNOWLEDGMENT

REFERENCES

1. Kristensen AS; Andersen J; Jorgensen TN; Sorensen L; Eriksen J; Loland CJ; Stromgaard K; Gether U, SLC6 Neurotransmitter Transporters: Structure, Function, and Regulation. Pharmacol. Rev 2011, 63, 585–640. [PubMed: 21752877]

2. Wang KH; Penmatsa A; Gouaux E, Neurotransmitter and Psychostimulant Recognition by the Dopamine Transporter. Nature 2015, 521, 322–327. [PubMed: 25970245]

3. Yamashita A; Singh SK; Kawate T; Jin Y; Gouaux E, Crystal Structure of a Bacterial Homologue of Na+/Cl--dependent Neurotransmitter Transporters. Nature 2005, 437, 215–223. [PubMed: 16041361]

4. Coleman JA; Green EM; Gouaux E, X-ray Structures and Mechanism of the Human Serotonin Transporter. Nature 2016, 532, 334–339. [PubMed: 27049939]

5. Singh SK; Piscitelli CL; Yamashita A; Gouaux E, A Competitive Inhibitor Traps LeuT in an Open-to-out Conformation. Science 2008, 322, 1655–1661. [PubMed: 19074341]

6. Beuming T; Kniazeff J; Bergmann ML; Shi L; Gracia L; Raniszewska K; Newman AH; Javitch JA; Weinstein H; Gether U; Loland CJ, The Binding Sites for Cocaine and Dopamine in the Dopamine Transporter Overlap. Nat. Neurosci. 2008, 11, 780–789. [PubMed: 18568020]

7. Bisgaard H; Larsen MA; Mazier S; Beuming T; Newman AH; Weinstein H; Shi L; Loland CJ; Gether U, The Binding Sites for Benztropines and Dopamine in the Dopamine Transporter Overlap. Neuropharmacology 2011, 60, 182–190. [PubMed: 20816875]

8. Plenge P; Mellerup ET, Antidepressive Drugs can Change the Affinity of [^{3}H]Imipramine and [^{3}H]Paroxetine Binding to Platelet and Neuronal Membranes. Eur. J. Pharmacol. 1985, 119, 1–8. [PubMed: 2935414]

9. Plenge P; Shi L; Beuming T; Te J; Newman AH; Weinstein H; Gether U; Loland CJ, Steric Hindrance Mutagenesis in the Conserved Extracellular Vestibule Impedes Allosteric Binding of Antidepressants to the Serotonin Transporter. J. Biol. Chem. 2012, 287, 39316–39326. [PubMed: 23007398]

10. Singh SK; Yamashita A; Gouaux E, Antidepressant Binding Site in a Bacterial Homologue of Neurotransmitter Transporters. Nature 2007, 448, 952–956. [PubMed: 17687333]

11. Zhou Z; Zhen J; Karpowich NK; Law CJ; Reith ME; Wang DN, Antidepressant Specificity of Serotonin Transporter Suggested by Three LeuT-SSRI Structures. Nat. Struct. Mol. Biol. 2009, 16, 652–657. [PubMed: 19430461]

12. Zhou Z; Zhen J; Karpowich NK; Goetz RM; Law CJ; Reith ME; Wang DN, LeuT-desipramine Structure Reveals How Antidepressants Block Neurotransmitter Reuptake. Science 2007, 317, 1390–1393. [PubMed: 17690258]

13. Wennogle LP; Meyerson LR, Serotonin Modulates the Dissociation of [3H]Imipramine from Human Platelet Recognition Sites. Eur. J. Pharmacol. 1982, 86, 303–7. [PubMed: 7160439]

14. Shi L; Quick M; Zhao Y; Weinstein H; Javitch JA, The Mechanism of a Neurotransmitter:Sodium Symporter--Inward Release of Na$^+$ and Substrate is Triggered by Substrate in a Second Binding Site. Mol. Cell 2008, 30, 667–677. [PubMed: 18570870]

15. Zhao Y; Terry DS; Shi L; Quick M; Weinstein H; Blanchard SC; Javitch JA, Substrate-Modulated Gating Dynamics in a Na$^+$-coupled Neurotransmitter Transporter Homologue. Nature 2011, 474, 109–113. [PubMed: 21516104]

16. Malinauskaite L; Quick M; Reinhard L; Lyons JA; Yano H; Javitch JA; Nissen P, A Mechanism for Intracellular Release of Na$^+$ by Neurotransmitter/Sodium Symporters. Nat. Struct. Mol. Biol. 2014, 21, 1006–1012. [PubMed: 25282149]

17. Stolzenberg S; Li Z; Quick M; Malinauskaite L; Nissen P; Weinstein H; Javitch JA; Shi L, The role of Transmembrane Segment 5 (TM5) in Na2 Release and the Conformational Transition of Neurotransmitter:Sodium Symporters toward the Inward-open State. J. Biol. Chem. 2017, 292, 7372–7384. [PubMed: 28320858]

18. Quick M; Abramyan AM; Wiriyasermkul P; Weinstein H; Shi L; Javitch JA, The LeuT-fold Neurotransmitter:Sodium Symporter MhsT has Two Substrate Sites. unpublished results.

19. Cartailler JP; Luecke H, Structural and Functional Characterization of π Bulges and Other Short Intrahelical Deformations. Structure 2004, 12, 133–144. [PubMed: 14725773]

20. Weyand S; Shimamura T; Yajima S; Suzuki S; Mirza O; Krusong K; Carpenter EP; Rutherford NG; Hadden JM; O'Reilly J; Ma P; Saidijam M; Patching SG; Hope RJ; Norbertczak HT; Roach PC; Iwata S; Henderson PJ; Cameron AD, Structure and molecular mechanism of a nucleobase-cation-symport-1 family transporter. Science 2008, 322, 709–713. [PubMed: 18927357]

21. Quick M; Winther AM; Shi L; Nissen P; Weinstein H; Javitch JA, Binding of an Octylglucoside Detergent Molecule in the Second Substrate (S2) Site of LeuT Establishes an Inhibitor-bound Conformation. Proc. Natl. Acad. Sci. U. S. A. 2009, 106, 5563–5568. [PubMed: 19307590]

22. Li Z; Lee AS; Bracher S; Jung H; Paz A; Kumar JP; Abramson J; Quick M; Shi L, Identification of a Second Substrate-Binding Site in Solute-Sodium Symporters. J. Biol. Chem. 2015, 290, 127–141. [PubMed: 25398883]

23. Zehnpfennig B; Wiriyasermkul P; Carlson DA; Quick M, Interaction of α-Lipoic Acid with the Human Na$^+$/Multivitamin Transporter (hSMVT). J. Biol. Chem. 2015, 290, 16372–16382. [PubMed: 25971966]

24. Sherman W; Day T; Jacobson MP; Friesner RA; Farid R, Novel Procedure for Modeling Ligand/ Receptor Induced Fit Effects. J. Med. Chem. 2006, 49, 534–553. [PubMed: 16420040]

25. Humphrey W; Dalke A; Schulten K, VMD: Visual Molecular Dynamics. J. Mol. Graphics 1996, 14, 33–38.

26. Phillips JC; Braun R; Wang W; Gumbart J; Tajkhorshid E; Villa E; Chipot C; Skeel RD; Kale L; Schulten K, Scalable Molecular Dynamics with NAMD. J. Comput. Chem. 2005, 26, 1781–1802. [PubMed: 16222654]

27. MacKerell AD; Bashford D; Bellott; Dunbrack RL; Evanseck JD; Field MJ; Fischer S; Gao J; Guo H; Ha S; Joseph-McCarthy D; Kuchnir L; Kuczera K; Lau FTK; Mattos C; Michnick S; Ngo T; Nguyen DT; Prodhom B; Reiher WE; Roux B; Schlenkrich M; Smith JC; Stote R; Straub J; Watanabe M; Wiórkiewicz-Kuczera J; Yin D; Karplus M, All-Atom Empirical Potential for Molecular Modeling and Dynamics Studies of Proteins†. J. Phys. Chem. B 1998, 102, 3586–3616. [PubMed: 24889800]

28. Best RB; Zhu X; Shim J; Lopes PE; Mittal J; Feig M; Mackerell AD, Jr., Optimization of the Additive CHARMM All-atom Protein Force Field Targeting Improved Sampling of the Backbone Φ, Ψ and Side-Chain X_1 and X_2 Dihedral Angles. J. Chem. Theory Comput 2012, 8, 3257–3273. [PubMed: 23341755]

29. Feller SE; Zhang Y; Pastor RW; Brooks BR, Constant Pressure Molecular Dynamics Simulation: The Langevin Piston Method. J. Chem. Phys. 1995, 103, 4613–4621.

30. Noé F; Horenko I; Schütte C; Smith JC, Hierarchical Analysis of Conformational Dynamics in Biomolecules: Transition Networks of Metastable States. J. Chem. Phys. 2007, 126, 04B617.

31. Prinz JH; Wu H; Sarich M; Keller B; Senne M; Held M; Chodera JD; Schutte C; Noe F, Markov Models of Molecular Kinetics: Generation and Validation. J. Chem. Phys. 2011, 134, 174105. [PubMed: 21548671]

32. Scherer MK; Trendelkamp-Schroer B; Paul F; Perez-Hernandez G; Hoffmann M; Plattner N; Wehmeyer C; Prinz JH; Noe F, PyEMMA 2: A Software Package for Estimation, Validation, and Analysis of Markov Models. J. Chem. Theory Comput 2015, 11, 5525–5542. [PubMed: 26574340]

33. Plattner N; Noe F, Protein Conformational Plasticity and Complex Ligand-Binding Kinetics Explored by Atomistic Simulations and Markov Models. Nat. Commun. 2015, 6, 7653. [PubMed: 26134632]

34. Wieczorek M; Sticht J; Stolzenberg S; Gunther S; Wehmeyer C; El Habre Z; Alvaro-Benito M; Noe F; Freund C, MHC Class II Complexes Sample Intermediate States along the Peptide Exchange Pathway. Nat. Commun. 2016, 7, 13224. [PubMed: 27827392]

35. Abramyan AM; Stolzenberg S; Li Z; Loland CJ; Noe F; Shi L, The Isomeric Preference of an Atypical Dopamine Transporter Inhibitor Contributes to Its Selection of the Transporter Conformation. ACS Chem. Neurosci. 2017, 8, 1735–1746. [PubMed: 28441487]

36. Perez-Hernandez G; Paul F; Giorgino T; De Fabritiis G; Noe F, Identification of Slow Molecular Order Parameters for Markov Model Construction. J. Chem. Phys. 2013, 139, 015102. [PubMed: 23822324]

37. Schwantes CR; Pande VS, Improvements in Markov State Model Construction Reveal Many Non-Native Interactions in the Folding of NTL9. J. Chem. Theory Comput. 2013, 9, 2000–2009. [PubMed: 23750122]

38. Noe F; Clementi C, Kinetic Distance and Kinetic Maps from Molecular Dynamics Simulation. J. Chem. Theory Comput 2015, 11, 5002–5011. [PubMed: 26574285]

39. Noe F; Nuske F, A Variational Approach to Modeling Slow Processes in Stochastic Dynamical Systems. Multiscale Model. Simul. 2013, 11, 635–655.

40. Nuske F; Keller BG; Perez-Hernandez G; Mey AS; Noe F, Variational Approach to Molecular Kinetics. J. Chem. Theory Comput. 2014, 10, 1739–1752. [PubMed: 26580382]

41. Swope WC; Pitera JW; Suits F, Describing Protein Folding Kinetics by Molecular Dynamics Simulations. 1. Theory. J. Phys. Chem. B 2004, 108, 6571–6581.

42. Roblitz S; Weber M, Fuzzy Spectral Clustering by PCCA Plus : Application to Markov State Models and Data Classification. Advances in Data Analysis and Classification 2013, 7, 147–179.

43. Verma RK; Abramyan AM; Michino M; Free RB; Sibley DR; Javitch JA; Lane JR; Shi L, The E2.65A Mutation Disrupts Dynamic Binding Poses of SB269652 at the Dopamine D2 and D3 Receptors. PLoS Comput. Biol. 2018, 14, e1005948. [PubMed: 29337986]

44. Stolzenberg S; Quick M; Zhao C; Gotfryd K; Khelashvili G; Gether U; Loland CJ; Javitch JA; Noskov S; Weinstein H; Shi L, Mechanism of the Association between Na$^+$ Binding and Conformations at the Intracellular Gate in Neurotransmitter:Sodium Symporters. J. Biol. Chem. 2015, 290, 13992–14003. [PubMed: 25869126]

45. McGibbon RT; Beauchamp KA; Harrigan MP; Klein C; Swails JM; Hernandez CX; Schwantes CR; Wang LP; Lane TJ; Pande VS, MDTraj: A Modern Open Library for the Analysis of Molecular Dynamics Trajectories. Biophys. J. 2015, 109, 1528–1532. [PubMed: 26488642]

46. Michino M; Boateng CA; Donthamsetti P; Yano H; Bakare OM; Bonifazi A; Ellenberger MP; Keck TM; Kumar V; Zhu C; Verma R; Deschamps JR; Javitch JA; Newman AH; Shi L, Toward Understanding the Structural Basis of Partial Agonism at the Dopamine D3 Receptor. J. Med. Chem. 2017, 60, 580–593. [PubMed: 27983845]

47. Quick M; Javitch JA, Monitoring the Function of Membrane Transport Proteins in Detergent-Solubilized Form. Proc. Natl. Acad. Sci. U. S. A. 2007, 104, 3603–3608. [PubMed: 17360689]

48. Schaffner W; Weissmann C, A Rapid, Sensitive, and Specific Method for the Determination of Protein in Dilute Solution. Anal. Biochem. 1973, 56, 502–514. [PubMed: 4128882]
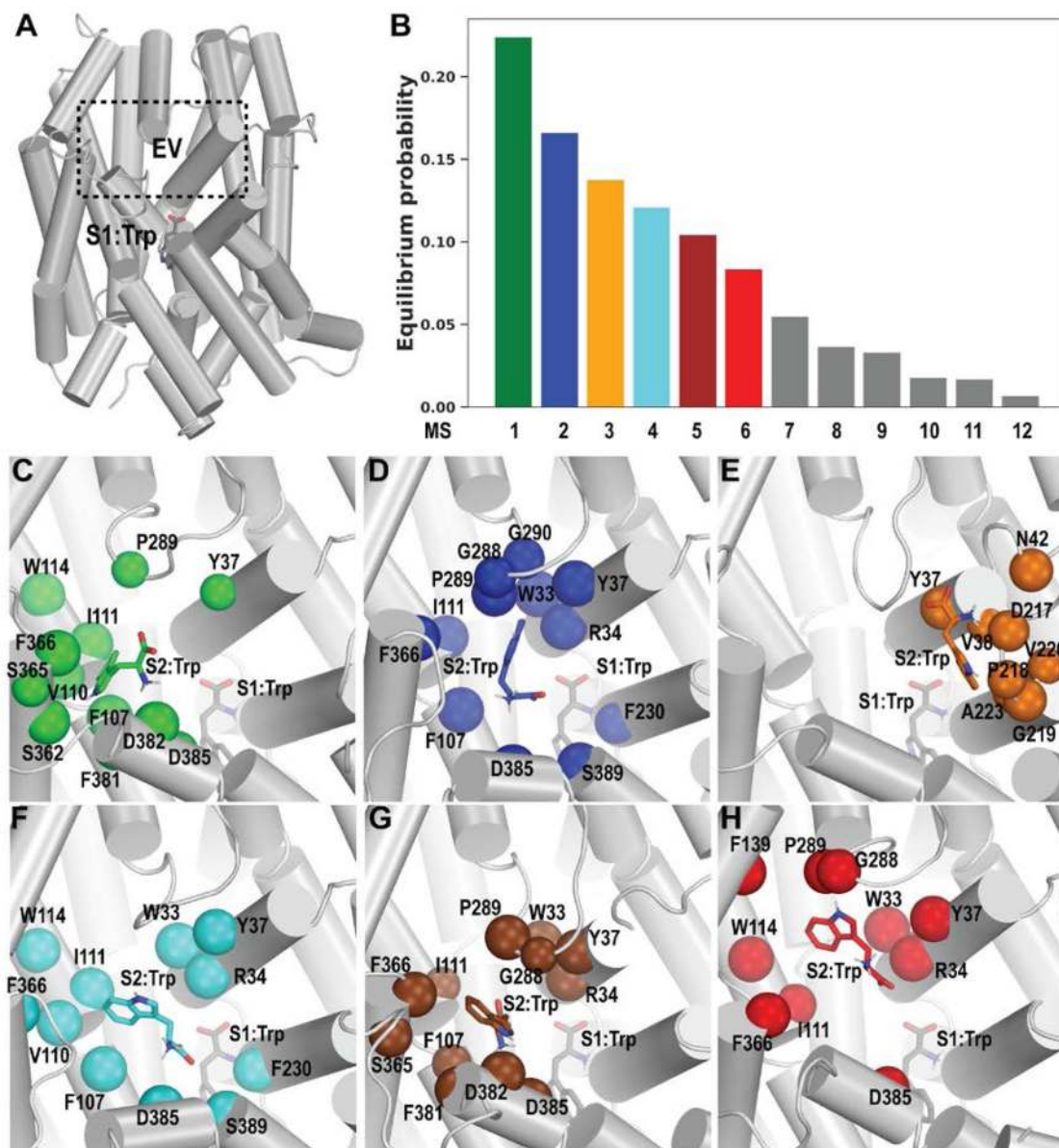
Figure 1.

MSM analysis of the MD simulations identified potential S2:Trp binding sites. (**A**) Side view of the MhsT structure (PDB ID: 4US3) showing the relative positions of the central S1 site and the EV. (**B**) Equilibrium probabilities of the MSs. The six MSs with largest equilibrium probabilities are colored, whereas the other MSs are in gray. **(C-H)** The S2:Trp binding poses in each of the six largest MSs, with the Cα atoms of S2:Trp interacting residues shown in spheres (colors correspond to those in panel B), the sizes of which are proportional to their interaction frequency with S2:Trp in each MS (see Table 1).
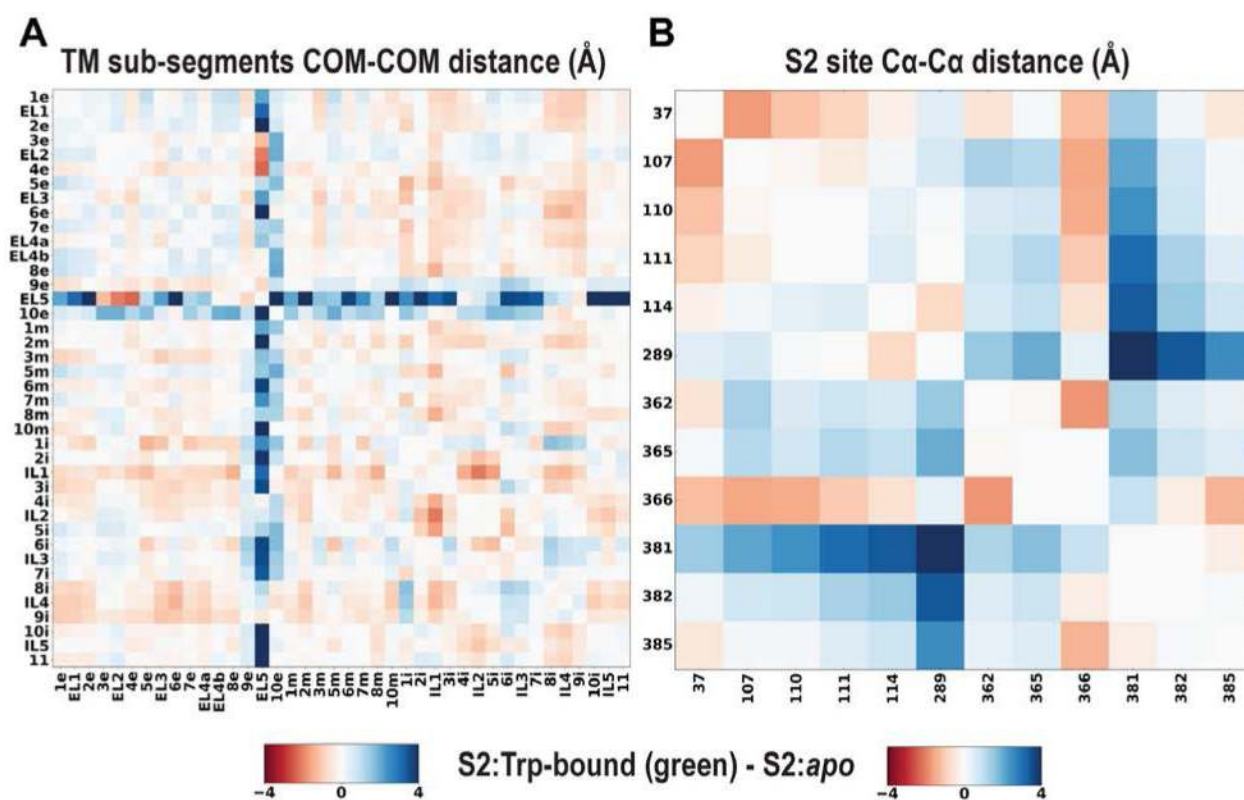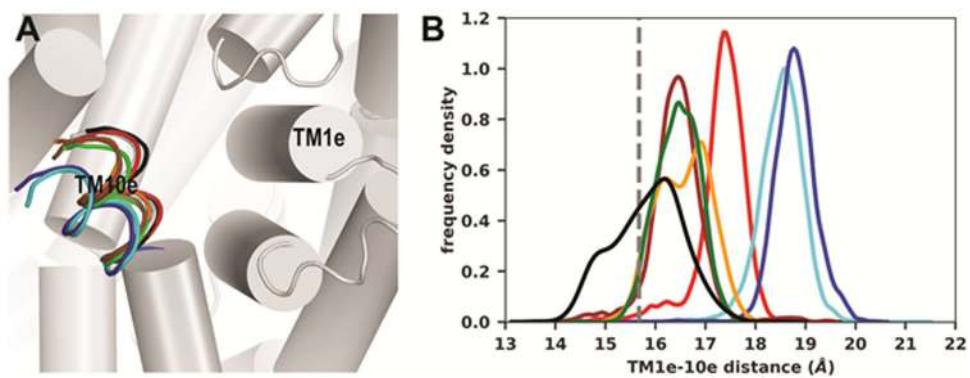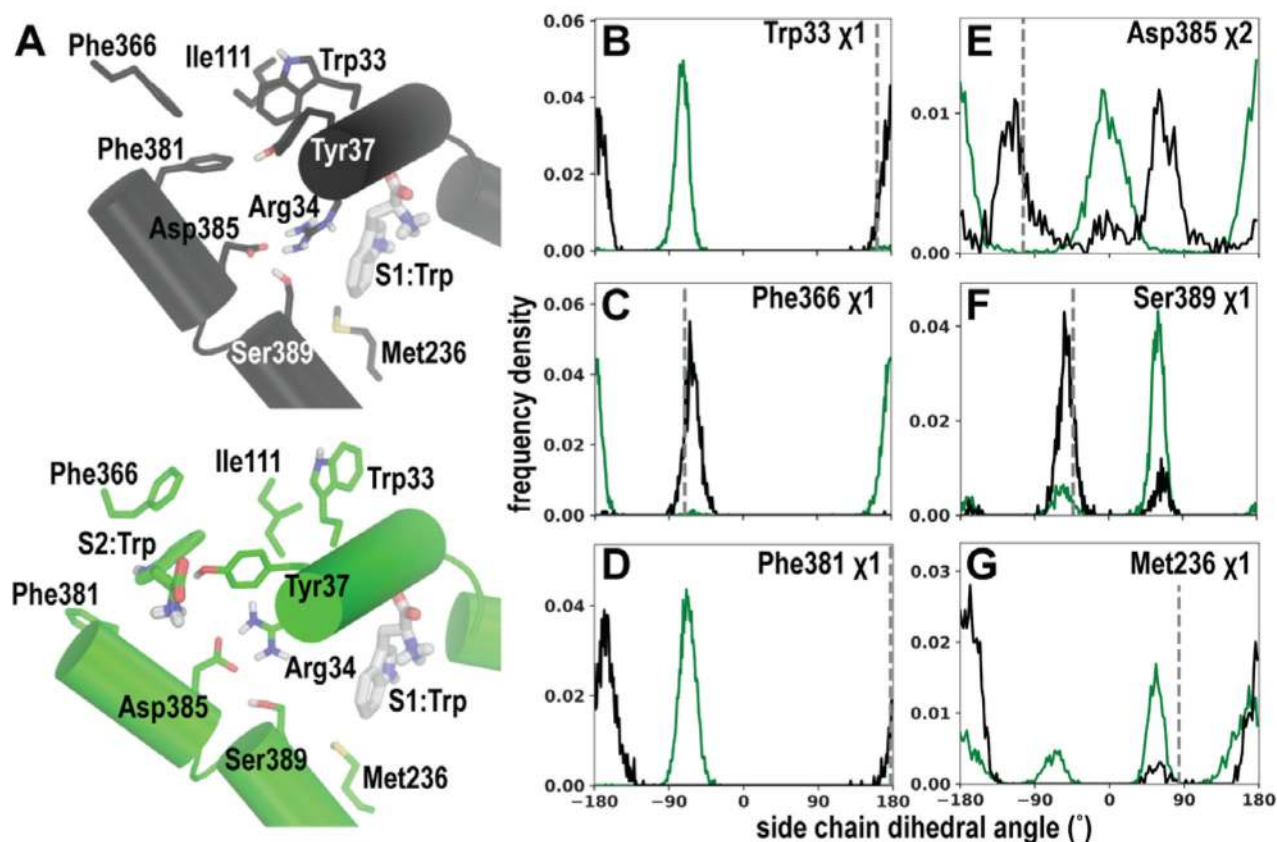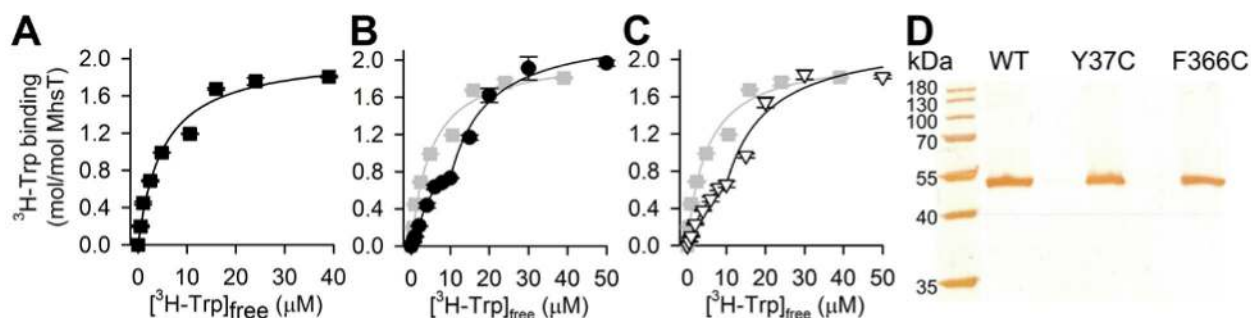
Figure 2.

The most dominant S2-bound MS (green) is characterized by outward movements of TM10e. **(A)** The pairwise distances among TM subsegments in the green MS are compared to those in the S2:*apo* condition.[17] The analysis highlights the conformational changes of TM10e and the neighboring EL5 in the green MS. **(B)** The pairwise Cα atom distances of the S2:Trp-interacting residues identified in the green MS (Table 1) are compared to those in the S2:*apo* condition. The results indicate significant changes of residues Phe366 (EL5) and Phe381 (TM10e) (see text).

Figure 3.
Conformational dynamics of TM10e in the S2-bound MSs. (A) A zoom-in view of the TM10e dynamics. **(B)** Distribution of the TM10e-TM1e distances. In both panels, the six MSs with largest equilibrium probabilities are colored in their respective colors as in Figure 1, the S2:*apo* condition is in black, and the crystal structure (PDB ID: 4US3) is in gray.
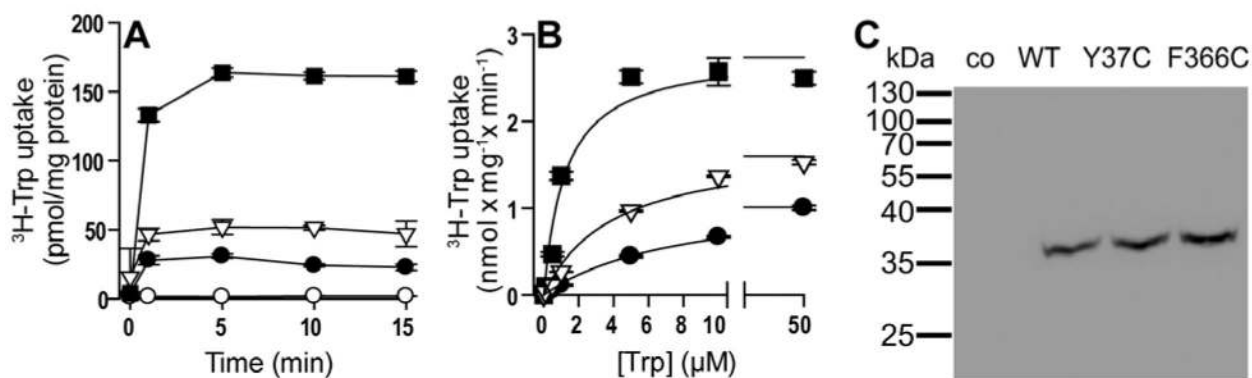
Figure 4.
Binding of S2:Trp in the green MS is associated with conformational changes that propagate towards the S1 site. (A) Compared to the S2:*apo* condition (upper panel), S2:Trp binding pose in the green MS (lower panel) is associated with different orientations of residues that propagate toward the S1 site. **(B-D)** The changes near the S2 site are demonstrated by different distributions of sidechain rotamers of Trp33, Phe366, and Phe381 in the green MS compared to those in the S2:*apo* condition (in black). **(E-G)** The propagation of the changes from the S2 to S1 site is demonstrated by different distributions of sidechain rotamers of Asp385, Ser389, and Met236 in the green MS compared to those in the S2:*apo* condition (in black). The values in the crystal structure (PDB ID: 4US3) are shown in gray dotted lines.

Figure 5.
Saturation equilibrium binding. 50 ng of purified protein was used with increasing concentrations (0.05–50 μM) of ^{3}H-Trp in the presence or 150 mM NaCl. **A**) Fitting the data for MhsT-WT to a rectangular hyperbola model revealed an EC_{50} of 7.5±1.0 μM. **B, C**) Data fitting for Y37C and F366C was performed in two steps[22]: fitting of the data between 0 and 10 μM ^{3}H-Trp to the Hill equation yielded an EC_{50} of 3.9±0.5 μM and 6.5±2.1 μM, with Hill coefficients of 1.7±0.3 and 1.3±0.2 (indicative of allosteric interactions involving more than one binding site) for Y37C and F366C, respectively, whereas fitting the data between 10 and 50 μM ^{3}H-Trp to a rectangular hyperbola model yielded an EC_{50} of 19.7±2.5 μM and 20.9±4.7 μM for Y37C and F366C, respectively. The molar binding ratio of Trp:MhsT-WT was 2.1±0.1, while it was 2.2±0.3 and 2.3±0.4 for Y37C and F366C, respectively. **D**) Purified MhsT variants (1 μg protein per lane) used for the equilibrium binding experiments were subjected to 11% SDS-PAGE followed by silver staining of the gel. The approximate molecular weight of the protein standard is indicated.

Figure 6.
^{3}H-Trp uptake. (A) Time course of Trp uptake. Uptake of 0.1 μM ^{3}H-Trp was measured in *E. coli* MQ614 expressing MhsT-WT (■), -Y37C (●), or -F366C (▽). MQ614 transformed with plasmid pQE60 (○) served as control. Data (mean ± S.E.M. of triplicate determinations) of a representative experiment (n ≥3) are shown. (B) Kinetics of the initial rates of ^{3}H-Trp transport (0.1 – 50 μM). Uptake was measured for periods of 10 s (WT) or 30 s (mutants). Data (mean ± S.E.M. of triplicate determinations) of a representative experiment (n=3) were fitted with the Michaelis-Menten nonlinear regression model. (C) Relative expression of MhsT variants. A monoclonal antibody against the N-terminal His tag in the MhsT variants was used to detect relative amounts of MhsT-WT, -Y37C, or -F366C in membrane vesicles of *E. coli* MQ614 cells in this representative Western blot. MQ614 transformed with pQE60 served as control (co).

Table 1.

S2:Trp-interacting residues in the six MSs with the largest equilibrium probabilities. In a MD frame, if the shortest heavy-atom distance between S2:Trp and any given residue of the protein was within 5Å, we defined that S2:Trp forms an interaction with this residue. The frequencies of interaction that are above 50% for each of the six MSs with the largest equilibrium probabilities are shaded in the corresponding MS colors. The equilibrium probability values for each MS are shown in the parenthesis.

		green (22.4%)	blue (16.6%)	orange (13.7%)	cyan (12.1%)	brown (10.4%)	red (8.3%)
TM1	TRP33	0.4	99.5	0.0	99.7	89.9	98.6
	ARG34	21.8	99.7	3.2	100.0	89.4	99.9
	TYR37	51.5	99.5	86.2	98.9	93.0	99.7
	VAL38	0.0	0.1	57.7	0.4	0.0	17.9
EL1	ASN42	0.0	0.0	84.1	0.0	0.0	0.0
TM3	PHE107	99.9	99.4	0.1	98.6	62.5	4.3
	VAL110	99.4	0.1	0.0	100.0	5.5	0.5
	ILE111	91.3	85.1	0.0	99.6	52.4	75.2
	TRP114	95.3	1.5	0.0	91.4	6.8	97.6
EL2	PHE139	0.0	0.1	6.7	0.0	0.8	99.9
EL3	ASP217	0.0	0.0	72.9	0.0	0.0	0.0
TM6	PR0218	0.0	0.0	59.6	0.0	0.0	0.0
	GLY219	0.0	0.0	84.1	0.0	0.0	0.0
	VAL220	0.0	0.0	53.0	0.0	0.0	0.0
	ALA223	0.0	0.0	87.2	0.0	0.0	0.0
	PHE230	0.0	69.6	0.0	85.6	1.6	0.0
EL4	GLY288	15.8	73.9	10.6	5.2	51.9	89.6
	PRO289	51.2	95.7	0.5	46.0	93.5	88.2
	GLY290	0.0	72.0	10.0	0.1	4.9	16.5
TM9	SER362	97.1	1.0	0.0	3.4	3.2	0.0
EL5	SER365	56.8	28.5	0.0	0.4	83.6	0.0
	PHE366	99.9	98.8	0.7	94.1	96.3	95.2
TM10	PHE381	97.4	1.3	1.0	0.4	97.5	14.4
	ASP382	99.9	1.5	13.3	0.7	97.1	7.8
	ASP385	86.5	99.7	4.0	100.0	93.3	76.7
	SER389	0.0	96.5	1.6	96.7	0.0	0.0